

Dissecting the Local Environment of FRB 190608 in the Spiral Arm of its Host Galaxy

JAY S. CHITTIDI,¹ SUNIL SIMHA,² ALEXANDRA MANNINGS,² J. XAVIER PROCHASKA,^{2,3} MARC RAFELSKI,^{4,5}
MARCEL NEELEMAN,⁶ JEAN-PIERRE MACQUART,⁷ NICOLAS TEJOS,⁸ REGINA A. JORGENSEN,¹ STUART D. RYDER,⁹
CHERIE K. DAY,^{10,11} LACHLAN MARNOCH,⁹ SHIVANI BHANDARI,¹¹ ADAM T. DELLER,¹⁰ HAO QIU,^{12,11}
KEITH W. BANNISTER,¹¹ RYAN M. SHANNON,¹⁰ AND KASPER E. HEINTZ¹³¹ *Maria Mitchell Observatory, 4 Vestal Street, Nantucket, MA 02554, USA*² *University of California - Santa Cruz, 1156 High St., Santa Cruz, CA, USA 95064*³ *Kavli Institute for the Physics and Mathematics of the Universe (Kavli IPMU), 5-1-5 Kashiwanoha, Kashiwa, 277-8583, Japan*⁴ *Space Telescope Science Institute, Baltimore, MD 21218, USA*⁵ *Department of Physics & Astronomy, Johns Hopkins University, Baltimore, MD 21218, USA*⁶ *Max-Planck-Institut für Astronomie, Königstuhl 17, D-69117, Heidelberg, Germany*⁷ *International Centre for Radio Astronomy Research, Curtin University, Bentley WA 6102, Australia*⁸ *Instituto de Física, Pontificia Universidad Católica de Valparaíso, Casilla 4059, Valparaíso, Chile*⁹ *Department of Physics & Astronomy, Macquarie University, NSW 2109, Australia*¹⁰ *Centre for Astrophysics and Supercomputing, Swinburne University of Technology, Hawthorn, VIC 3122, Australia*¹¹ *Australia Telescope National Facility, CSIRO Astronomy and Space Science, PO Box 76, Epping, NSW 1710, Australia*¹² *Sydney Institute for Astronomy, School of Physics, the University of Sydney, NSW 2007, Australia*¹³ *Centre for Astrophysics and Cosmology, Science Institute, University of Iceland, Dunhagi 5, 107 Reykjavík, Iceland*

ABSTRACT

We present a high-resolution analysis of the host galaxy of fast radio burst FRB 190608, an SBc galaxy at $z = 0.11778$ (hereafter HG 190608), to dissect its local environment and its contributions to the FRB properties. Our Hubble Space Telescope WFC3/UVIS image reveals that the sub-arcsecond localization of FRB 190608 is coincident with a knot of star-formation ($\Sigma_{\text{SFR}} = 1.2 \times 10^{-2} \text{ M}_{\odot} \text{ kpc}^{-2}$) in one of the prominent spiral arms of HG 190608. This is confirmed by $\text{H}\beta$ emission present in our Keck/KCWI integral field spectrum of the galaxy with a surface brightness of $\mu_{\text{H}\beta} = (3.35 \pm 0.18) \times 10^{-17} \text{ erg s}^{-1} \text{ cm}^{-2} \text{ arcsec}^{-2}$. We infer an extinction-corrected $\text{H}\alpha$ surface brightness and compute a dispersion measure from the interstellar medium of HG 190608 of $\text{DM}_{\text{Host,ISM}} = 82 \pm 35 \text{ pc cm}^{-3}$. The galaxy rotates with a circular velocity $v_{\text{circ}} = 141 \pm 8 \text{ km s}^{-1}$ at an inclination $i_{\text{gas}} = 37 \pm 3^{\circ}$, giving a dynamical mass $M_{\text{halo}}^{\text{dyn}} \approx 10^{11.96 \pm 0.08} \text{ M}_{\odot}$. A surface photometric analysis of the galaxy using FORS2 imaging suggests a stellar disk inclination of $i_{\text{stellar}} = 26 \pm 3^{\circ}$. The dynamical mass estimate implies a halo contribution to the dispersion measure of $\text{DM}_{\text{Host,Halo}} = 55 \pm 25 \text{ pc cm}^{-3}$ subject to assumptions on the density profile and fraction of baryons retained. The relatively high temporal broadening ($\tau = 3.3 \pm 0.2 \text{ ms}$ at 1.28 GHz) and rotation measure ($\text{RM} = 353 \pm 2 \text{ rad m}^{-2}$) (Day et al. 2020) of FRB 190608 may be attributable to both turbulent gas within the spiral arm and gas local to the FRB progenitor. In contrast to previous high-resolution studies of FRB progenitor environments, we find no evidence for disturbed morphology, emission, nor kinematics for FRB 190608.

Keywords: galaxies: distances and redshifts, spiral arms, star formation, stars: general, radio transient source

1. INTRODUCTION

Fast radio bursts (FRBs) are brief ($\delta t \sim \text{ms}$) pulses of bright ($\gtrsim 1 \text{ Jy ms}$) radio emission detected primarily

at meter and decimeter wavelengths (Petroff et al. 2019; Cordes & Chatterjee 2019). While similar in nature to pulsars and their cousins – the rotating radio transients (RRATs), the energetics and stochastic repeating nature of (at least) some FRBs imply a qualitatively distinct physical mechanism (Platts et al. 2019). Discovered over a decade ago, the frequent localization of these

sources is a recent advance enabled by new facilities, operational modes, and extensive follow-up campaigns (e.g. Bannister et al. 2019; Ravi et al. 2019; Chatterjee et al. 2017). Approximately 7 events with arcsecond or sub-arcsecond localizations are now associated to their host galaxies, providing first assessments of the population (see Bhandari et al. 2020; Macquart et al. 2020; Marcote et al. 2020, and references therein). This first set shows a diversity of galaxy properties, with stellar masses ranging from $M_\star \approx 10^8 - 10^{11} M_\odot$, specific star formation rates spanning from $\text{sSFR} \approx 10^{-8} \text{ yr}^{-1}$ to less than 10^{-11} yr^{-1} , and morphologies ranging from spiral to dwarf to early-type systems.

As demonstrated by studies of gamma-ray bursts (GRBs, e.g. Bloom et al. 2002; Prochaska et al. 2006), a promising path forward to understanding the origin of transient sources is to dissect the galaxies that host them, i.e. constraining/understanding the typical mass, SFR, environment, etc. of galaxies hosting FRBs. While GRBs were early on linked to supernovae (SNe), which pinpointed their explosion mechanism, FRBs thus far have no detected associated transient counterparts (Marnoch & Ryder 2020). Instead, we have to rely on the host and FRB properties for insight into the progenitor(s). For GRBs, the former were central to implicating the collapsar model as the progenitor of long-duration bursts (Fruchter et al. 2006). This followed from both the association of these GRBs to star-forming galaxies and that they were typically co-located with the brightest region of UV emission within the galaxy.

Galaxy properties and the local FRB environment may inform both progenitor models and other scientific pursuits with FRBs (Eftekhari & Berger 2017; Tendulkar et al. 2017; Prochaska & Zheng 2019; Bhandari et al. 2020). These include the star-formation rate, the morphology of both gas and stars, the metallicity, and the location of the event relative to the galaxy nucleus, its stellar distribution, and its interstellar medium. Estimating these properties requires deep imaging and multi-wavelength spectra at high spatial-resolution combined with a high-precision localization. Assessing whether FRBs are produced in specific regions or in distinct small-scale environments will ultimately provide prominent constraints on the progenitor models.

Previous works have examined the environments of two repeating FRBs with milliarcsecond localizations from very-long-baseline interferometry (VLBI) measurements (FRBs 121102 and 180916.J0158+65; Tendulkar et al. 2017; Marcote et al. 2020). FRB 121102 was identified with a nebular region in a dwarf, low metallicity, star-forming galaxy and is nearly coincident with a per-

sistent radio source. These associations have inspired and supported FRB models related to young, massive stars in metal-poor environments and to scenarios that invoke active galactic nuclei (AGN) activity (Zhang & Wang 2019; Katz 2017; Vieyro et al. 2017). In contrast, FRB 180916.J0158+65 lies in the outer arm of a more massive, spiral galaxy, with an overall low star-formation rate. Repeating FRBs thus appear to not favor any distinct environments (and/or show a broad range of galaxy environments).

In this study, we focus on an apparently non-repeating event, FRB 190608, discovered and localized with the Australian Square Kilometer Array Pathfinder (ASKAP) (Macquart et al. 2020). Its host galaxy, identified as SDSS J221604.90-075356.0 and hereafter called HG 190608, is also a spiral galaxy with high stellar mass ($M_\star \approx 10^{10.4} M_\odot$) and a star formation rate $\text{SFR} \approx 1.2 M_\odot \text{ yr}^{-1}$ (Bhandari et al. 2020). Full analysis of the FRB base-band data (Day et al. 2020), yields a dispersion measure $\text{DM}_{\text{FRB}} = 339.79 \text{ pc cm}^{-3}$, a rotation measure $\text{RM}_{\text{FRB}} = 353 \pm 2 \text{ rad m}^{-2}$, and a scattering time of $\tau = 3.3 \pm 0.2 \text{ ms}$ at 1.28 GHz. The DM value, when corrected for Galactic contributions, exceeds the average cosmic value by nearly a factor of two (Macquart et al. 2020), indicating either a large host contribution and/or an over-density of foreground gas (Simha et al. 2020). Meanwhile, the RM and τ measurements respectively indicate a magnetized plasma foreground to FRB 190608 and suggest propagation through a turbulent medium. The primary motivation for this manuscript is to examine the environment of FRB 190608 in the context of these propagation effects.

To this end, we have obtained UV imaging of HG 190608 with the *Hubble Space Telescope* (HST) at a spatial resolution of full width at half maximum (FWHM) $\approx 0.1''$. These data are complemented by integral field spectroscopic observations with the Keck Cosmic Web Imager on the Keck II telescope. The resultant data cube maps the nebular emission lines across the galaxy, albeit at seeing-limited ($\approx 0.9''$) resolution. Together, these data are used to explore and constrain the physical environment of FRB 190608.

This paper is organized as follows. We detail the datasets and their reduction in Section 2. Section 3 provides the primary measurements of the dataset, including kinematic modeling of the galaxy. We then consider how the host galaxy may contribute to the dispersion measure, rotation measure, and scattering observed for the FRB in Section 4. Finally, we discuss our results by comparing to the spiral host galaxy of FRB 180916.J0158+65 (Marcote et al. 2020) in Section 5 and summarize our work in Section 6. Throughout this work,

we have assumed cosmological parameters from the results of [Planck Collaboration et al. \(2016\)](#).

2. DATA

2.1. ASKAP

At Coordinated Universal Time (UT) 22:48:12 on 2019 June 08, FRB 190608 was detected by the Comensal Real-time ASKAP Fast Transients (CRAFT) survey on the Australian Square Kilometer Array Pathfinder (ASKAP) and was subsequently localized to 22h16m04.77s, $-07^{\circ}53'm53.7s$ (right ascension, declination, J2000).

The high-time resolution analysis in [Day et al. \(2020\)](#) yielded a more precise FRB localization than reported in [Macquart et al. \(2020\)](#). The statistical uncertainty in the position is described by an ellipse with $\sigma_{\text{RA,Stat}} = 0.19''$ for one axis and $\sigma_{\text{Dec,Stat}} = 0.18''$ for the other. In addition, the registration of the ASKAP image in the International Celestial Reference Frame is subject to an uncertainty determined by the number and brightness of background radio sources present in the image. This systematic uncertainty is estimated to be an ellipse with $\sigma_{\text{RA,Sys}} = 0.18''$ and $\sigma_{\text{Dec,Sys}} = 0.18''$. The errors along respective axes are added in quadrature for a final FRB position uncertainty (68% c.l.) with a semi-major axis (RA) of $\sigma_{\text{RA}} \approx 0.26''$ and a semi-minor axis (Dec) of $\sigma_{\text{DEC}} \approx 0.25''$.

The dispersion measure of FRB 190608 is measured at $\text{DM}_{\text{FRB}} = 339.79 \text{ pc cm}^{-3}$ ([Day et al. 2020](#)), well exceeding the Galactic ISM estimate along its sightline ($\text{DM}_{\text{MW,ISM}} \approx 33 \text{ pc cm}^{-3}$; [Cordes & Lazio 2002](#)).

Analysis of the base-band data reveals a large rotation measure ([Day et al. 2020](#)): $\text{RM} = 353 \pm 2 \text{ rad m}^{-2}$. Furthermore, the observed pulse is broad ($\approx 3.3 \text{ ms}$ at 1 GHz) and shows a roughly ν^{-4} dependence. For the following, we assume a scatter broadening of $\approx 2 \text{ ms}$ ([Day et al. 2020](#)). These measurements respectively indicate propagation through magnetized and turbulent plasma.

2.2. HST/UVIS Observations and Reduction

On UT 2019 Oct 11, we obtained near-ultraviolet imaging with the Wide Field Camera 3 (WFC3) on the *Hubble Space Telescope* (HST). We used the wide F300X filter, covering rest-frame $\sim 2400 - 3200 \text{ \AA}$. While this filter has a red tail out to $\sim 4000 \text{ \AA}$, it has a high UV throughput of $\sim 15\%$ with a wide pass-band. The single orbit was divided into 4×600 second exposures. To minimize the effects from charge transfer degradation and maximize UV sensitivity, the target was placed near the readout on chip 2 on amplifier C, and the exposures include $9e^-$ postflash per exposure to reach a $12e^-$

per pixel background. The images are dithered with a box dither pattern 5 times larger than the standard WFC3/UVIS box dither pattern to minimize residual background patterns.

The four images are calibrated with custom processing similar to that described in [Rafelski et al. \(2015\)](#), which will be described in more detail in Prichard et al. in prep. In short, we use a new correction for charge transfer efficiency, use concurrent dark exposures for superdark creation, equalize the number of hot pixels detected as a function of distance to the readout, and normalize the amplifiers to each other. The near-UV images are combined using *AstroDrizzle* ([Avila et al. 2015](#)) at their native 40 mas plate scale with a pixel fraction of 0.8, include sky subtraction, and are oriented North up and East left. The images are aligned to GAIA DR2 ([Gaia Collaboration et al. 2018](#)) using *TweakReg* ([Avila et al. 2015](#)) and have an astrometric accuracy of $\approx 0.02''$. Figure 1 presents the combined image and the FRB localization.

2.3. SDSS

The localization of FRB 190608 associates it to a galaxy cataloged by the Sloan Digital Sky Survey, SDSS J221604.90-075356.0. The SDSS spectrum recorded from the inner $3''$ -diameter of the galaxy yields a redshift $z = 0.11778$. Figure 2 shows a portion of the SDSS spectrum focusing on a series of standard nebular lines. In addition to the narrow nebular emission characteristic of star-forming regions, the data also show broad H α emission indicative of a Type 1 AGN ([Stern & Laor 2012](#)). [Bhandari et al. \(2020\)](#) further analyzed this spectrum and the SDSS photometry to estimate a stellar mass $M_{\star} \approx 10^{10.4} M_{\odot}$, $\text{SFR} \approx 1.2 M_{\odot} \text{ yr}^{-1}$, and metallicity $Z = 0.009$.

2.4. Keck/KCWI Observations and Reduction

On UT 2019 Sep 30 and Oct 01, we obtained a combined set of 3×900 second exposures of HG 190608 with the Keck Cosmic Web Imager (KCWI) on the Keck II telescope. The data were obtained with the integral field unit (IFU) in the “Medium” slicer position with the “BM” grating, resulting in a field-of-view (FOV) of $16.5'' \times 20.4''$ and a spectral resolution of $R=5000$ (FWHM). Both observing nights were clear with seeing of $\text{FWHM} \sim 0.9''$.

The data were processed with the standard KCWI Data Reduction Pipeline¹ ([Morrissey et al. 2018](#)). Flat field and arc calibrations were made using data from the

¹ <https://github.com/Keck-DataReductionPipelines/KcwiDRP>

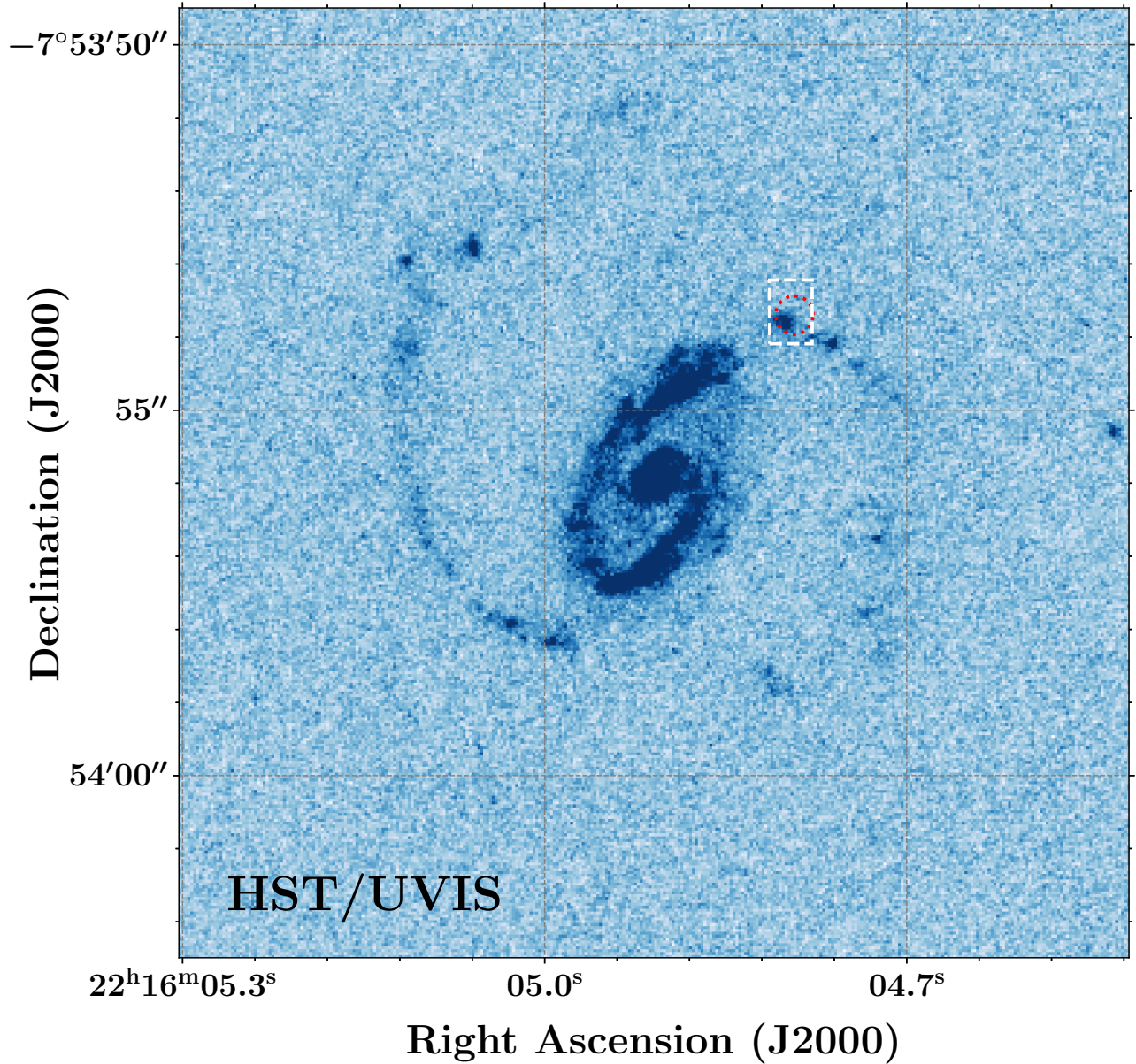


Figure 1. The *HST/UVIS* F300X image of HG 190608. The galaxy shows a bulge and prominent spiral characteristic of an SBc galaxy. The 1σ uncertainty in the FRB position (red oval) is coincident with a star-formation region in the NW spiral arm. We estimate a surface brightness of $\mu_{\text{UV}} \approx (4.65 \pm 0.18) \times 10^{-3} \text{ mJy arcsec}^{-2}$ within the red ellipse. The dashed-white box represents the region evaluated in the KCWI analysis.

September 30th run. Sky subtraction sampling was limited to slices beyond the host galaxy to avoid subtracting any signal in the spectra. The pipeline also corrected for differential atmospheric refraction across the field-of-view. Finally we flux calibrate the spectra with standard star observations of BD+25 4655 and G191B2B with the same configuration as for the host galaxy observations.

The three exposures were aligned and combined to increase the signal-to-noise using the *CWITools*² package (O’Sullivan et al. 2019), and rebinned so both spatial axes are in the same scale. Each spaxel covers a projected size of $0.29'' \times 0.29''$. We then converted the wavelengths from air to vacuum and applied a geomotion correction based on the sightline and time of observation. Given the absence of any other bright source in

² *CWITools*: <https://github.com/dbosul/CWITools>

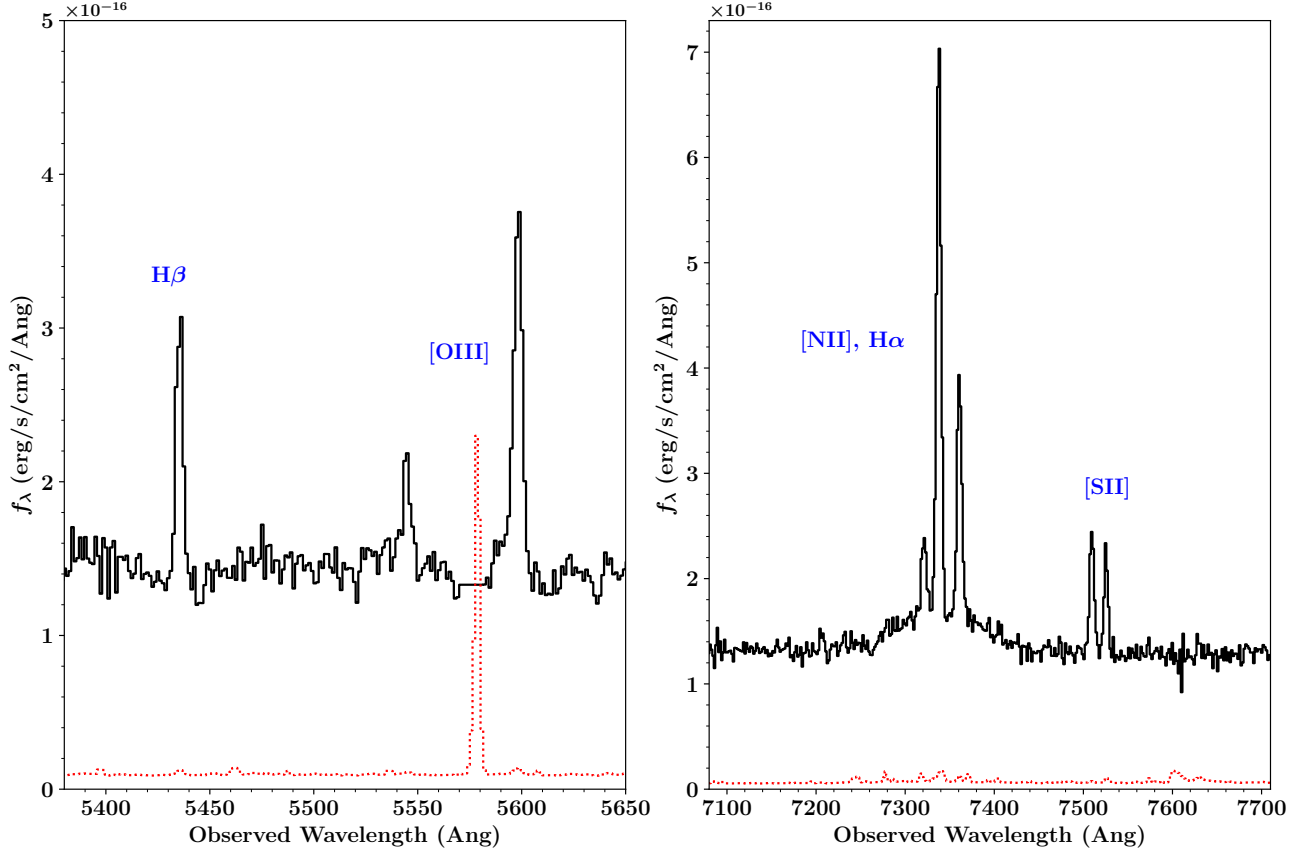


Figure 2. Portions of the SDSS spectrum of HG 190608 centered on standard nebular emission lines. Note the broad H α emission underneath the narrow H α and [NII] emission are hallmarks of a Type 1 AGN.

the KCWI FoV, we have forced the astrometric solution of HG 190608 from SDSS to the centroid of the KCWI data identified with intensity contours and estimate an uncertainty on the order of half a spaxel ($\sim 0.15''$).

3. MEASUREMENTS

3.1. *HST*/UVIS Imaging

In Figure 1, we present the processed *HST*/UVIS image with the FRB localization indicated by the red circle. Its centroid lies just off of bright UV emission associated with the NW spiral arm, which is encompassed by the 68% position uncertainty. We classify the host as a grand design SBc galaxy based on the bright, bar-like ring of star formation connecting the relatively small bulge to the two spiral arms. We attribute the tightly-wound inner structure to star-formation near the inner Lindblad resonance with the bar (Schommer & Sullivan 1976; Elmegreen 1994; Englmaier & Shlosman 2000).

We estimate the galaxy center from the flux-weighted centroid of the UV flux within the bulge and find a position of 22h16m04.90s, $-07^{\circ}53'55.91''$ (RA, Dec) with a statistical uncertainty of $0.08''$. Two methods of determining the centroid (`photutils.centroids.centroid_com`

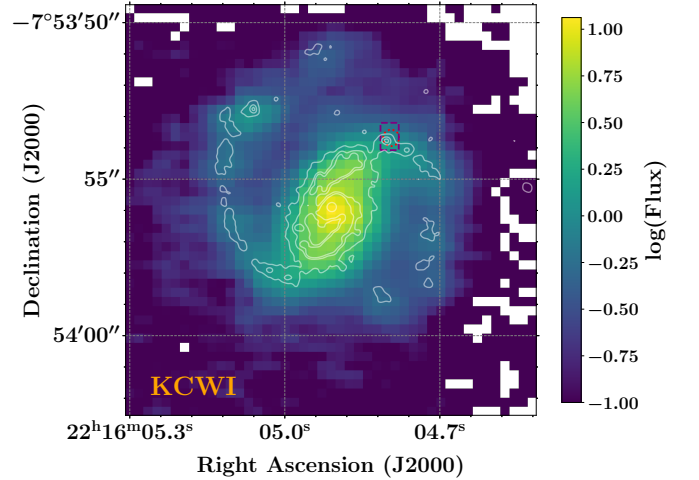


Figure 3. A pseudo-narrowband H β image of HG 190608 created by summing the KCWI spaxels between $\lambda_{\text{obs}} \approx 5425.4 - 5445.4\text{\AA}$. Linear contours from the Gaussian-smoothed *HST* data are overlaid in white. The $1-\sigma$ uncertainty in the FRB position is overlaid in red, and the 6 spaxel box used for flux measurements is shown by the dashed-purple rectangle.

and `photutils.centroids.centroid_1dg`) agree to within 1 pixel ($0.04''$), providing our estimate of the systematic uncertainty. This yields a projected offset of $2.93'' \pm 0.28''$ for FRB 190608 from the center of the galaxy with the uncertainty dominated by the systematic error of the FRB localization. At $z = 0.11778$, this corresponds to a projected physical offset of $R_{\perp} = 8.03 \pm 0.77$ kpc, consistent with the estimate of Bhandari et al. (2020).

Within the FRB positional uncertainty (see red oval in Figure 1), we measure an integrated UV electron flux (number of electrons accumulated in the detector) of 1.457 ± 0.050 $\text{e}^- \text{s}^{-1}$. The uncertainty is determined by taking the inverse square root of the inverse sensitivity map, a data product from the *HST/UVIS* pipeline. Adopting the AB magnitude zeropoint ($ZP_{\text{F300X}} = 25.069$) for the F300X filter (Dressel 2019), we determine a UV flux of $f_{\nu, \text{UV}} = (3.11 \pm 0.12) \times 10^{-4}$ mJy ($m_{\text{AB}} = 25.2$) and subsequently a UV surface brightness of $\mu_{\text{UV}} = (4.65 \pm 0.18) \times 10^{-3}$ mJy arcsec $^{-2}$.

3.2. Keck/KCWI Line Fluxes

Complementing the *HST* observations, the KCWI data cube yields measurements on the nebular emission lines within the rest-frame interval $\lambda_{\text{rest}} \approx 4723 - 5577 \text{\AA}$. Figure 3 shows a pseudo narrow-band image of HG 190608 centered on $\text{H}\beta$ emission ($\lambda_{\text{obs}} \approx 5425.4 - 5445.4 \text{\AA}$). Overlaid on the $\text{H}\beta$ pseudo-image are the contours of UV emission from the *HST* image. As expected, there is a close correspondence between the two; the KCWI data is effectively a seeing-smoothed description of the star-forming regions.

We define a 6 spaxel region encompassing the 1σ localization circle of FRB 190608 (see the purple box in Figure 3) from which we extract a 1D-spectrum to analyze the $\text{H}\gamma$, $\text{H}\beta$, and $[\text{O III}]$ 4959 emission lines. The $[\text{O III}]$ 5007 was beyond the acceptable wavelength range due to our instrument configuration. We measured line fluxes by fitting a Gaussian to each line and estimate uncertainties by subtracting the Gaussian fits from the data and then calculating the standard deviation of the residual spectrum. This method yielded uncertainties about an order of magnitude higher than the formal errors from the fit. Figure 4 shows the emission lines and fits and Table 1 reports the measurements.

From the ratio of $\text{H}\gamma$ to $\text{H}\beta$ flux at the FRB position, we can estimate the internal reddening from dust in the galaxy. Comparing the observed ratio 0.392 to the theoretical value of 0.466 from Osterbrock & Ferland (2006) and adopting the extinction curve from Cardelli et al. (1989), we estimate $A_V = 1.00$ mag. This is comparable to the extinction estimate of Bhandari et al. (2020)

from their analysis of the SDSS spectrum from the inner region.

From the $\text{H}\beta$ line flux and the area of the integration region, we determine an average $\text{H}\beta$ surface brightness of $\mu_{\text{H}\beta} = (3.35 \pm 0.18) \times 10^{-17}$ erg $\text{s}^{-1} \text{cm}^{-2} \text{arcsec}^{-2}$, uncorrected for dust. We may also estimate the dust-corrected $\text{H}\alpha$ surface brightness $\mu_{\text{H}\alpha}^{\text{corr}}$, as follows. We adopt the observed $\text{H}\beta$ surface brightness and the estimated internal extinction A_V . We assume the intrinsic $f_{\text{H}\alpha}/f_{\text{H}\beta}$ follows the putative ratio of 2.87 for H II regions (Osterbrock & Ferland 2006) and find that $f_{\text{H}\alpha}/f_{\text{H}\beta} = 3.95$. This yields $\mu_{\text{H}\alpha}^{\text{corr}} = (29.2 \pm 1.6) \times 10^{-17}$ erg $\text{s}^{-1} \text{cm}^{-2} \text{arcsec}^{-2}$.

The measured line fluxes at the FRB location show a lower $[\text{O III}]/\text{H}\beta$ ratio than through the SDSS fiber on the central regions, which may be explained by the presence of AGN emission in the nucleus (as also indicated by the broad $\text{H}\alpha$ emission component). To explore this further, we generated a flux-ratio image by fitting each $[\text{O III}]$ and $\text{H}\beta$ emission line with a Gaussian and integrating to determine the flux (rather than direct integration which produced a noisier result). Only spaxels that had a signal-to-noise ratio > 3 for both $\text{H}\beta$ and $[\text{O III}]$ are plotted in Figure 5. We find that the central region of the galaxy has an $[\text{O III}]/\text{H}\beta$ ratio of ≈ 0.5 while the FRB region is ≈ 0.4 .

3.3. Keck/KCWI Kinematics

In Figure 6, we present a map of the ionized gas kinematics of HG 190608 – the velocity δv relative to $z = 0.11778$ and the RMS velocity dispersion σ – as measured from the KCWI data. To determine the gas velocities, we used a Gaussian model to fit the $\text{H}\beta$ lines detected at each spaxel, with the rest wavelength determined by the redshift. The data reveal rotation characteristic of a disk galaxy, with the region presumed to host the FRB – in the north-west spiral arm – approaching us while the south-east spiral arm is receding. On the assumption the arms are trailing, the FRB would therefore lie within the near side of the galaxy disk as seen from Earth. However, the prominent inner region revealed in the *HST/UVIS* data in Figure 1 consists of a tight spiral or “ring” that may be associated with gas compression and star formation driven by the inner Lindblad resonance. The inclination of the bulge, the spiral arms, and the outer stellar disk may all be different, suggesting a warped disk. We explore this further in Section 3.3.1.

To calculate the velocity dispersion, we subtract off the instrumental velocity dispersion of 25.5 km s^{-1} in quadrature. We observe a sharp peak in dispersion at the center of the galaxy of $\approx 108 \text{ km s}^{-1}$, consistent with

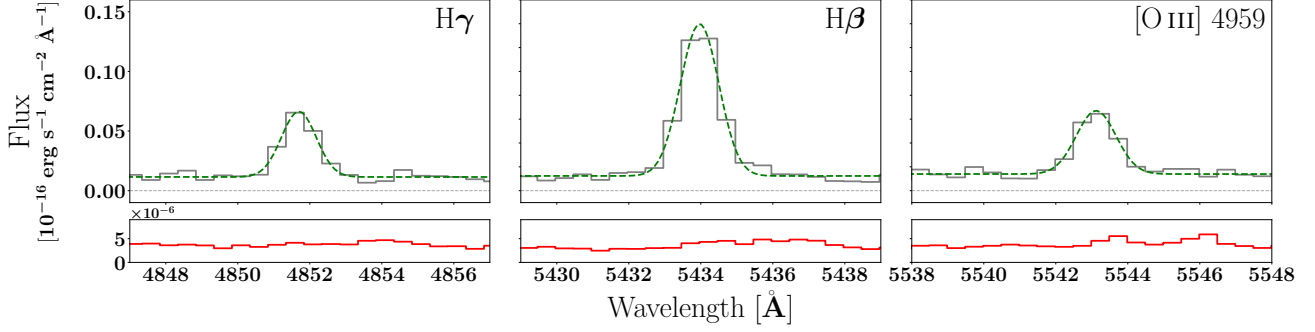


Figure 4. Summed spectra of the 2×3 spaxel box at the FRB position for each identified emission line. The gray solid lines are the spectra, the green dashed lines are the fitted Gaussians to each line, the dotted gray lines show the zero-level flux, and the solid red lines are the variance.

Table 1. HG 190608 Emission Line Measurements

Line	λ_{rest}^c (Å)	KCWI FRB Position ^a	SDSS ^b
		Line Flux ($10^{-17} \text{ erg s}^{-1} \text{ cm}^{-2}$)	Line Flux ($10^{-17} \text{ erg s}^{-1} \text{ cm}^{-2}$)
H γ	4341.68	0.67 ± 0.05	39.2 ± 3.4
H β	4862.68	1.71 ± 0.09	83.7 ± 3.3
[O III] 4959	4960.295	0.73 ± 0.05	50 ± 2
H α	6564.61	—	277 ± 4.15

^aMeasured from the 6 spaxels encompassing the FRB position (See Figure 3)

^bMeasurements taken from Bhandari et al. (2020)

^cVacuum wavelengths adopted from <http://classic.sdss.org/dr6/algorithms/linestable.html>

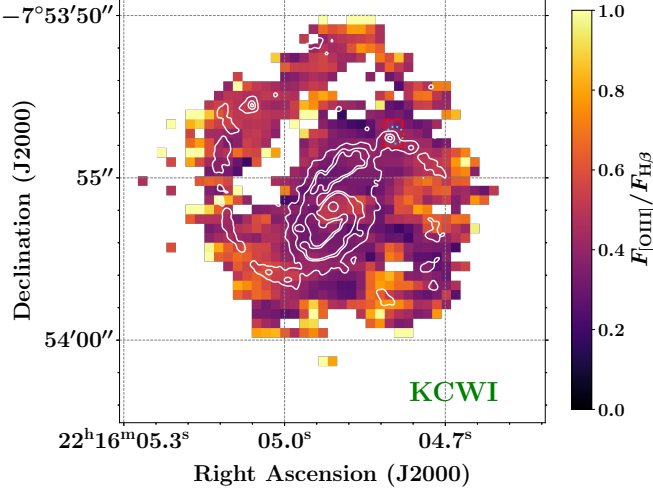


Figure 5. Map of the ratio of [O III] and H β flux. Each emission line above a $3\text{-}\sigma$ detection was fitted with a Gaussian to determine the flux. Like Figure 3, contours from the *HST* data are overlaid in white, the dashed-red rectangle is a box used for measurements regarding the FRB position, and the cyan-dashed circle is the 1σ uncertainty in the FRB position.

the dispersion measured in the SDSS spectrum ($110.85 \pm 11.492 \text{ km s}^{-1}$), that falls more quickly along the major axis than the minor axis.

Averaging the velocity and velocity dispersion images over the 6 spaxel box covering the FRB uncertainty region, we estimate $\delta v = -79 \pm 0.52 \text{ km s}^{-1}$ (relative to $z = 0.11778$) and $\sigma = 15 \pm 0.55 \text{ km s}^{-1}$. Reported uncertainties were determined by the Gaussian fit parameters for the H β emission line. At the FRB position, we observe no peculiar velocity behavior when compared to a similar position along the SE spiral arm.

3.3.1. Spiral Galaxy Model

To estimate kinematical parameters for HG 190608, such as its rotational velocity and intrinsic velocity dispersion, we model the H β emission line data using the python-based code `qubefit`³ (Neeleman et al. 2019). This code fits the continuum-subtracted H β data cube to a model data cube generated from a user-defined model which is convolved with the point spread function and line spread function of the instrument. This three-dimensional approach minimizes biases in the kinematical properties of the galaxy caused by the finite resolution of the instrument and observations (e.g. Di Teodoro & Fraternali 2015). The best-fit parameters and associated uncertainties are determined by the code through a

³ <https://github.com/mneeleman/qubefit>

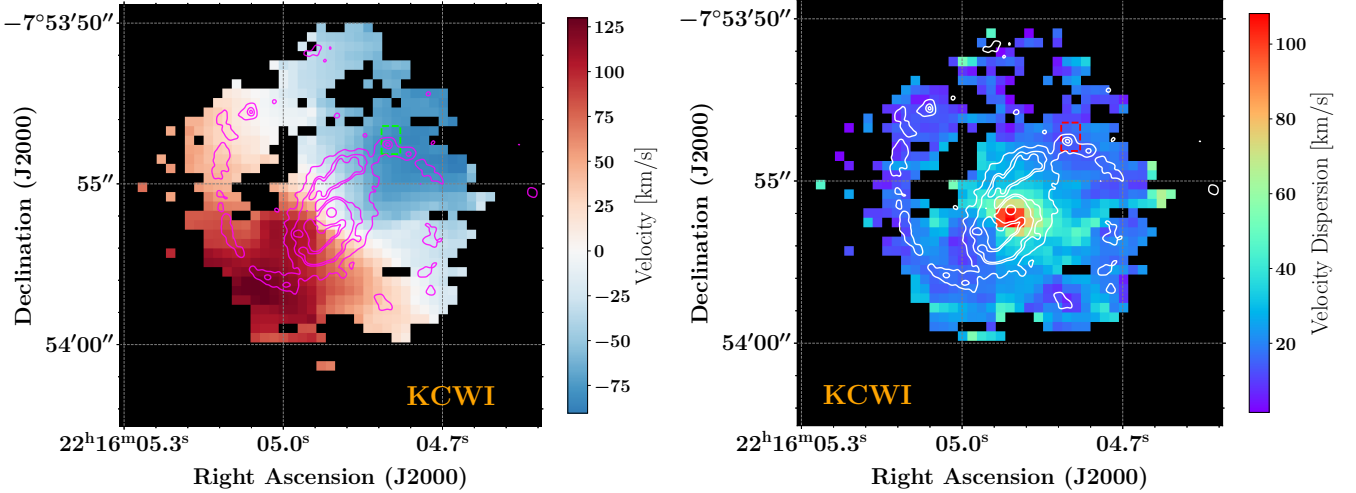


Figure 6. Left: A Doppler-velocity map of the KCWI data with the zero-point set by the SDSS redshift. Spaxels for which we have at least a $3\text{-}\sigma$ detection of the $\text{H}\beta$ line are fit with a Gaussian. We adopt the central wavelength of the fit and compute the velocity for each spaxel. We overlaid the contours from the *HST* data in magenta and the dashed-green rectangle is the 2×3 spaxel box which we averaged to compute the velocity at the FRB position. Right: A velocity dispersion map of the KCWI data showing only spaxels with a $3\text{-}\sigma$ detection of $\text{H}\beta$. We subtracted the dispersion of 25.5 km s^{-1} resulting from the resolution of the instrument configuration (Morrissey et al. 2018). The *HST* contours are in white and the dashed-red rectangle is the region over which we computed the average dispersion for the FRB position.

Markov Chain Monte Carlo approach, whereby the parameter space is sampled using an affine-invariant sampler, *emcee* (Foreman-Mackey et al. 2013). Flat priors are assumed for all parameters.

As HG 190608 shows two distinct spiral arms, we took the thin and thick disk galaxy models described in Neeleman et al. (2019) and added in a spiral density wave described by a Gaussian profile in the azimuthal direction whose central position, ψ_c , varies with radius, r , according to: $\psi_c(r) = \psi_{c,0} + k * r$, where k describes the tightness of the spiral structure and $\psi_{c,0}$ the position of the spiral structure at the center. Finally, the $\text{H}\beta$ intensity of the spiral structure was taken to obey a simplified step function with a constant value for the intensity, I_s , below the cut-off radius of the spiral, r_s . This spiral model adds 4 additional parameters to the thin and thick disk models.

We ran fits for both the thin and thick disk models using 300 walkers and 1000 runs each. Results of the fitting are given in Table 2. The best fit models yield an inclination angle of $i \approx 37 \pm 3^\circ$, where we have adopted the average result of the two models and an uncertainty that is inclusive of both results. We also find a circular rotation speed corrected for the inclination of $v_{\text{circ}} = 141 \pm 8\text{ km s}^{-1}$ between the two models. These values are in good agreement with the results obtained using the three-dimensional tilted-ring fitting routine, *3DBarolo* (Di Teodoro & Fraternali 2015). This code uses a series of concentric rings to estimate the kinematics of each ring and is therefore sensitive to poten-

tial warps of the gas disk. However, no such warps were observed in the ionized gas of HG 190608. Using the pixel-by-pixel normalization in *3DBarolo*, we determine an inclination and circular rotation speed of 37° and 170 km s^{-1} , respectively.

The inferred $v_{\text{circ}} = 141 \pm 8\text{ km s}^{-1}$ allows us to estimate a dynamical mass for the dark matter halo based on the simple model of Mo et al. (1998), as $M_{\text{halo}}^{\text{dyn}} \approx 0.1G^{-1}H^{-1}(z)v_{\text{circ}}^3$, where G is the gravitational constant and $H(z)$ is the Hubble parameter at redshift z . We obtain $M_{\text{halo}}^{\text{dyn}} \approx 10^{11.96 \pm 0.08} M_\odot$, which is consistent with the inferred halo mass from abundance matching (see Section 4.1).

3.4. Optical Surface Photometric Analysis

Figure 6 highlights how dependent the kinematical analysis presented in Section 3.3.1 is to the presence and strength of ionized gas. However, the influence of the bar and streaming motions along the arms means this model may not truly reflect the inclination of the underlying stellar or neutral gas disks. A deep *g*-band image of HG 190608 obtained with the FORS2 camera on the Very Large Telescope is presented in Bhandari et al. (2020). We carried out a surface photometry analysis on this image using the *isophot* tools within V3.17 of the STSDAS package in V2.16 of IRAF⁴. This fits elliptical isophotes to galaxy images, varying the photo-

⁴ <https://ascl.net/9911.002>

Table 2. Kinematic Modeling Results

Parameter	Units	Thin Disk Model	Thick Disk Model
i_{gas}^a	($^\circ$)	$39.19^{+0.62}_{-0.49}$	$35.70^{+0.17}_{-0.17}$
α^b	($^\circ$)	$133.05^{+0.95}_{-0.33}$	$135.55^{+0.15}_{-1.77}$
I_0^c	(10^{-16} erg s $^{-1}$ cm $^{-2}$ Å $^{-1}$ arcsec $^{-2}$)	$159.91^{+4.70}_{-11.46}$	$143.37^{+86.49}_{-36.38}$
R_d^d	(kpc)	$2.48^{+0.31}_{-0.17}$	$2.66^{+0.12}_{-0.16}$
Z_f^e	(kpc)	-	$0.09^{+0.03}_{-0.05}$
v_{circ}^f	(km s $^{-1}$)	$146.14^{+2.24}_{-4.96}$	$140.39^{+6.11}_{-7.02}$
σ_v^g	(km s $^{-1}$)	$34.62^{+1.09}_{-1.20}$	$38.16^{+1.61}_{-2.29}$
$\phi_{c,0}^h$	($^\circ$)	$110.38^{+1.24}_{-1.37}$	$103.28^{+5.45}_{-1.28}$
k^i	-	$-0.20^{+0.00}_{-0.00}$	$-0.20^{+0.00}_{-0.00}$
D_ϕ^j	($^\circ$)	$1.81^{+1.13}_{-1.16}$	$3.08^{+1.56}_{-0.38}$
I_s^k	-	$1.35^{+1.72}_{-0.67}$	$0.74^{+0.65}_{-0.25}$
r_s^l	(kpc)	$14.99^{+0.91}_{-0.59}$	$14.53^{+0.39}_{-0.16}$

^aInclination.^bPosition angle.^cCentral specific flux per PSF area.^dExponential scale length.^eThickness of disk; relevant only for the Thick Disk Model.^fCircular velocity.^gVelocity dispersion.^hCentral position of spiral structure.ⁱTightness of spiral structure.^jThickness of spiral arms.^kFraction of central intensity for spiral structure.^lCutoff radius of spiral arms.

metric centre coordinates (X,Y), ellipticity e ($= 1 - b/a$, where a and b are the ellipse semi-major and semi-minor axis lengths, respectively) and position angle θ , using the iterative method of [Jedrzejewski \(1987\)](#).

A first pass allowed all parameters to vary, but showed the photometric centre to be consistent to <0.5 pixel. On the next pass, the centre was held fixed and only e and θ allowed to vary. Within a radius of $4''$, the bar dominates with large e , while beyond $\sim 7''$ both e and θ undergo wild swings as the surface brightness drops well below the sky level. Between these regimes we find $e = 0.10 \pm 0.02$, corresponding to an inclination $i_{stellar} = (26 \pm 3)^\circ$.

The difference in derived gas and stellar inclinations is small but significant. A direct correction of the circular rotation speed would imply $v_{circ} \approx 194$ km s $^{-1}$ and $M_{halo}^{dyn} \approx 10^{12.38} M_\odot$. However, since the fitting algorithm discussed in the previous section was applied to a gas emission line, a correction using $i_{stellar}$ may not yield as realistic a solution as separately fitting the stellar kinematics.

4. FRB PROPAGATION

In this section, we analyze our measurements of the local environment to provide context to the FRB measurements.

Table 3. Relevant and Derived Quantities

Parameter	Value	Reference
DM _{FRB}	339.79 pc cm $^{-3}$	Day et al. (2020)
RM _{FRB}	353 ± 2 rad m $^{-2}$	Day et al. (2020)
M_\star	$10^{10.4} M_\odot$	Bhandari et al. (2020)
v_{circ}	141 ± 8 km s $^{-1}$	This Work
$f_{[O III]}/f_{H\beta}$	0.43	This Work
$f_{H\alpha}/f_{H\beta}$	3.95	This Work
A_V	1.00	This work
i_{gas}	$37 \pm 3^\circ$	This work
$i_{stellar}$	$26 \pm 3^\circ$	This work
M_{halo}^{dyn}	$10^{11.96 \pm 0.08} M_\odot$	This work
DM _{Host}	137 ± 43 pc cm $^{-3}$	This work
Σ_{SFR}	$1.2 \times 10^{-2} M_\odot \text{ yr}^{-1} \text{ kpc}^{-2}$	This work

4.1. DM_{Host}

[Prochaska & Zheng \(2019\)](#) detail how the dispersion measure of FRBs may probe the cosmic web once one accounts for contributions from the Milky Way and the FRB host galaxy. The latter, in particular, is poorly constrained and may be the dominant systematic to any such DM analysis ([Macquart et al. 2020](#)).

Here we estimate the host contribution, DM_{Host}, to the total FRB dispersion measure, DM_{FRB}, from (1)

gas in the star-forming ISM of HG 190608 ($DM_{\text{Host,ISM}}$) and (2) unseen gas from its galactic halo ($DM_{\text{Host,Halo}}$).

For the former, we follow the procedure outlined in Tendulkar et al. (2017) and references therein (Reynolds 1977; Cordes et al. 2016). This requires an estimate of the $H\alpha$ emission measure $EM_{H\alpha}$ at the FRB position. From the dust-corrected $H\alpha$ surface brightness $(29.2 \pm 1.6) \times 10^{-17} \text{ erg s}^{-1} \text{ cm}^{-2} \text{ arcsec}^{-2}$ at the FRB location (see Section 3.2), we estimate $EM_{H\alpha} = 222 \pm 12 \text{ pc cm}^{-6}$ (Reynolds 1977). We then adopt Equation 5 from Tendulkar et al. (2017) to estimate $DM_{\text{Host,ISM}}$ in the observer frame:

$$DM_{\text{Host,ISM}} \approx 387 \text{ pc cm}^{-3} L_{\text{kpc}}^{1/2} \left[\frac{f_f}{\zeta(1+\epsilon^2)/4} \right]^{1/2} \times \left(\frac{EM}{600 \text{ pc cm}^{-6}} \right)^{1/2} \times (1+z)^{-1} \quad (1)$$

where f_f is the volume filling-factor, ϵ represents the variation *within* any given cloud of ionized gas due to turbulence, and ζ is the density variation *between* any two clouds, all over a pathlength of L_{kpc} (Reynolds 1977; Cordes et al. 2016; Tendulkar et al. 2017).

We assume that each ionized cloud along our line-of-sight has internal density variations dominated by turbulence ($\epsilon=1$) and that there is total variation between clouds ($\zeta=2$). Finally, we assume that the FRB resides in the midplane of the spiral arm in which the thin disk scale height is similar to the half width at half maximum (HWHM) of the Milky Way thin disk detected by H I gas ($L_{\text{kpc}} = 0.150$; Kalberla & Kerp 2009) and dominates the contribution to $DM_{\text{Host,ISM}}$. Using our $EM_{H\alpha}$ estimate, we obtain an ISM contribution of $82 \pm 19 \text{ pc cm}^{-3}$ with the quoted uncertainty solely from statistical uncertainty in the flux measurements. We estimate a systematic uncertainty of $\sim 30 \text{ pc cm}^{-3}$ based on our ignorance of ϵ, ζ , and L and our assumptions to infer $f_{H\alpha}$. Altogether, we estimate $DM_{\text{Host,ISM}} = 82 \pm 35 \text{ pc cm}^{-3}$.

This $DM_{\text{Host,ISM}}$ estimate has adopted the average surface brightness in the $\approx 0.58'' \times 0.87''$ area encompassing the FRB localization. Figure 1 shows that the spiral arms exhibit significant structure within this region. Specifically, we measure a peak flux in the integration box that is ≈ 1.5 times the average value. If FRB 190608 occurred at the peak location, we would estimate a $DM_{\text{Host,ISM}}$ value that is $\approx 20\%$ higher, comparable to the statistical error.

Xu & Han (2015) used the framework of NE2001 to model dispersion measures of FRBs originating from a spiral galaxy at varying inclination. The resulting posterior distribution was fit with a skew Gaussian, and for a 40° inclination, they reported a peak DM of 47 pc cm^{-3}

with a right HWHM extending to 90 pc cm^{-3} , inclusive with our estimate.

Ionized gas within the halo of HG 190608 will contribute an additional factor $DM_{\text{Host,Halo}}$ to DM_{Host} . We estimate this contribution as follows. Starting from the stellar mass estimate of HG 190608, we implement the abundance matching technique to infer a halo mass of $M_{\text{halo}} = 10^{11.9} M_\odot$ (Moster et al. 2013). This mass is consistent with the dynamical mass estimated in Section 3.3.1. We can then estimate $DM_{\text{Host,Halo}}$ by assuming a density profile for the halo gas. For a fiducial estimate, we assume that the halo has retained all of its cosmic fraction of baryons and that $f_{\text{hot}} = 75\%$ of these are in the halo as ionized gas. We further assume the modified Navarro-Frenk-White (NFW) profile described by Prochaska & Zheng (2019) and that the halo terminates at a radius of $r = 10 \text{ kpc}$, with the gas within dominated by the galaxy ISM (and $DM_{\text{Host,ISM}}$). Last, we adopt an impact parameter $R_\perp = 8.03 \text{ kpc}$ and place the galaxy at the center of the halo such that the sightline to FRB 190608 intersects only one half.

Altogether, we estimate $DM_{\text{Host,Halo}} = 49 \text{ pc cm}^{-3}$ in our observer frame. This estimate bears significantly more uncertainty than the semi-empirical $DM_{\text{Host,ISM}}$ estimate. First, errors in the stellar mass and dispersion in the abundance matching relation imply an $\approx 0.2 \text{ dex}$ uncertainty in M_{halo} and an $\approx 20\%$ uncertainty in $DM_{\text{Host,Halo}}$. Substantially steeper density profiles, strongly disfavored by simulations of galaxy formation and low X-ray emission from spiral galaxies, would allow for a $DM_{\text{Host,Halo}}$ up to 100% larger. Lastly, the halo may be deficient in baryons with $f_{\text{hot}} \ll 0.75$. Altogether, we suggest a range $DM_{\text{Host,Halo}} = 30 - 80 \text{ pc cm}^{-3}$ ($55 \pm 25 \text{ pc cm}^{-3}$).

Combining with our empirical estimate for $DM_{\text{Host,ISM}}$, we estimate $DM_{\text{Host}} = 137 \pm 43 \text{ pc cm}^{-3}$. This is $\approx 25 - 50\%$ of DM_{FRB} and likely at least 50% of the value corrected for the Galaxy.

4.2. Scattering

Day et al. (2020) measured the scattering timescale of the burst by fitting a Gaussian intrinsic profile convolved with the approximately exponential tail expected of temporal smearing by an inhomogeneous cold plasma. The burst profile was fit as a function of frequency across seven subbands covering the bandwidth range 1105-1433 MHz. The authors found that the observed frequency-dependent burst profile can be adequately fit by a single Gaussian component of constant width modified by frequency-dependent scattering, where the scattering timescale follows a power-law with frequency as $\tau = (3.3 \pm 0.2) (\nu/1280 \text{ MHz})^{-3.5 \pm 0.9} \text{ ms}$ (Day et al. 2020).

The index of the scattering and its error are consistent with scattering by Kolmogorov turbulence at the $1\text{-}\sigma$ level (index = -4.4) or with scattering where the diffractive scale is below the inner (dissipation) scale of the turbulence at the $1\text{-}\sigma$ level (index = -4.0). The index is consistent to $2\text{-}\sigma$ with the average index measured for pulsar lines-of-sight in our galaxy (Bhat et al. 2004). We interpret the result in terms of scattering by a Kolmogorov spectrum of density inhomogeneities for ease of comparison against the properties of the interstellar medium of our own Galaxy.

The measured scattering timescale cannot be explained by scattering in our Galaxy, being three to four orders of magnitude larger than expected at the observed Galactic latitude of -48.6° (Cordes & Lazio 2002).

However, the magnitude of the scattering is problematically large if attributed to the interstellar medium of the host galaxy. One would expect the host galaxy to contribute an amount of temporal smearing comparable to the Milky Way given the low inclination of HG 190608 ($37 \pm 3^\circ$), the burst location in an outer spiral arm, and the fact that the gas mass of the host is comparable to the Milky Way. If the burst is in the midplane of the host galaxy, its sightline would be equivalent to sightlines in the Milky Way at Galactic latitudes $\gtrsim 50^\circ$, for which the scattering measure is $\text{SM} < 10^{-3.7} \text{ kpc m}^{-20/3}$.

Nonetheless, the derived scattering measure is $\text{SM} = 1.4(D_{\text{eff}}/1 \text{ kpc})^{-5/6} \text{ kpc m}^{-20/3}$, where we have conservatively assumed a fiducial effective distance to the scattering medium of $D_{\text{eff}} \sim 1 \text{ kpc}$ from the burst location.

The relationship between dispersion measure and scattering measured for pulsars in the Milky Way (Bhat et al. 2004; Krishnakumar et al. 2015) provides an independent means to estimate the expected amount of scattering based on the estimated host DM contribution. Using the estimated upper bound of $\text{DM}_{\text{Host,ISM}} = 82 \pm 19 \text{ pc cm}^{-3}$ and ignoring any negligible contribution from the much sparser gas in the halo, we estimate a temporal smearing timescale of $3 \mu\text{s}$.

The discrepancy between the observed smearing timescale and these various estimates of the expected host galaxy ISM contribution leads us to conclude either that:

- the scattering instead arises in an exceptionally turbulent and dense medium associated either with the burst/circumburst medium or a dense H II region in the spiral arm of the host galaxy or;
- the scattering arises at cosmological distances due to some turbulent intervening structure, where the

large effective scattering distance alleviates the requirement of a large scattering measure (since $\tau \propto D_{\text{L}}D_{\text{LS}}/D_{\text{S}}$, where D_{S} and D_{L} are the angular diameter distances to the source and scattering plane, respectively, and D_{LS} is the distance between the source and scattering plane).

We discuss each of these possibilities in turn.

(i) We consider whether the burst could originate in an especially turbulent and dense region. Any such association plausibly confines any putative scattering region to $D_{\text{eff}} < 10 \text{ pc}$, which requires $\text{SM} > 65 \text{ kpc m}^{-20/3}$. Scattering that is yet more local to the burst would imply an even higher constraint on the scattering measure. We remark that the observed scattering is 2.5 orders of magnitude greater than that observed in any analogous system observed in our Galaxy: the most extreme scattering environment observed in the Milky Way is associated with an energetic neutron star – the Crab nebula – whose scattering reaches values of $600 \mu\text{s}$ at 610 GHz (McKee et al. 2018), equivalent to 15 microseconds at 1.4 GHz .

The scattering could instead originate from the chance intersection of a dense, turbulent H II region associated with the line-of-sight. We regard this as the most plausible option. However, we note that the scattering measure is comparable to the highest values encountered in our own Galaxy – notably those toward the Galactic Centre, whose scattering is attributed to an H II region $\approx 2 \text{ kpc}$ from Earth (Dexter et al. 2017).

(ii) The scattering could be associated with structure in the cosmic web along the line-of-sight. Regarding the diffuse IGM, Simha et al. (2020) have performed a reconstruction of the cosmic web and report no evidence for a large concentration of matter along this line-of-sight. Regarding scattering from the gas in intervening galactic halos, Simha et al. (2020) report only a single halo is intercepted along the sightline (at $z = 0.09$) and estimate its scattering contribution to be $\tau_{\text{halo}} \lesssim 0.1 \text{ ms}$. Therefore, it is improbable that the cosmic web dominates the inferred scattering of FRB 190608.

4.3. Rotation Measure

FRB 190608 has one of the larger rotation measures recorded for an FRB to date ($\text{RM} = 353 \pm 2 \text{ rad m}^{-2}$, Day et al. 2020), requiring a highly magnetized plasma along the sightline. The estimate for the Milky Way Galactic halo at this high Galactic latitude is $\text{RM}_{\text{MW}} = -25 \pm 8 \text{ rad m}^{-2}$ (Oppermann et al. 2012); therefore, we expect the signal is dominated by an extragalactic component.

We identify four possible origins for the high observed RM:

- a foreground galaxy or halo in the line-of-sight,
- the host galaxy ISM, without a large-scale magnetic field,
- large-scale magnetic fields in the host disk and/or halo, or
- a dense and turbulent medium in which the burst could potentially be produced.

We examine each scenario below.

(i) Highly-magnetized foreground material could plausibly produce the observed high RM. However, [Simha et al. \(2020\)](#) estimated a negligible contribution to the RM ($< 1 \text{ rad m}^{-2}$) from their analysis of the intervening halos along the FRB 190608 sightline, leaving the host and local environment as the most likely suspects.

(ii) A high degree of regularity, over large scales, in the magnetic fields threading the host galaxy ISM could be responsible for the high observed RM. Analysis of magnetic field strengths (via rotation measures) from spiral arms in the outer disk of the Milky Way yield a characteristic $|\text{RM}| \approx 180 \text{ rad m}^{-2}$ ([Brown & Taylor 2001](#)). However, we note this estimate was based on observations made at low galactic latitudes, and this need not apply to the observed rotation measure in a roughly face-on spiral galaxy as in the case of HG 190608. The findings in [Fletcher et al. \(2011\)](#) of the magnetic field in M51, a face-on spiral galaxy ($i = (22 \pm 5)^\circ$, [Colombo et al. 2014](#)), are more relevant. The authors found rotation measures outside of the galaxy center in the disk to be generally $|\text{RM}| < 100 \text{ rad m}^{-2}$ and the total magnetic field strengths to be strongest in the interarm regions ($10\text{--}15 \mu\text{G}$, [Beck 2015](#)) rather than in the arms. We note that the authors found no organizing field or pattern to the RM, i.e. no large-scale magnetic field present.

M51 also has Σ_{SFR} an order of magnitude higher than HG 190608 ([Leroy et al. 2017](#)). This corresponds to a lower expected thermal electron density, lower magnetic field, and a lower RM in HG 190608. Furthermore, turbulent cells in the host ISM along the line-of-sight would reduce the contributed RM by a factor of \sqrt{N} , where N is the number of cells. For cell sizes of $\sim 50 \text{ pc}$ ([Fletcher et al. 2011](#)), we can expect the RM contribution of the ISM to be reduced by a factor of ~ 2 .

Thus, for the host galaxy ISM to dominate the observed RM, the magnetic field would have to be somewhat larger (and/or remain ordered on larger physical scales) than the Milky Way or M51, albeit only by a factor of a few.

(iii) While M51 lacks a large-scale magnetic field, [Mora-Partiarroyo et al. \(2019\)](#) found that a phenomenon

known as “magnetic ropes” could produce such a field, as in the edge-on spiral galaxy NGC 4631. A regular magnetic field with a strength of $\approx 4 \mu\text{G}$ oriented out of the plane of the galaxy was observed, with $|\text{RM}|$ as high as 400 rad m^{-2} in some regions. If a similar phenomenon is present in HG 190608, we can estimate the magnetic field strength parallel to the sightline as:

$$B_{\parallel} = 9.2 \mu\text{G} \left(\frac{\text{RM}}{353 \text{ rad m}^{-2}} \right)^{-1} \left(\frac{n_e}{0.05 \text{ cm}^{-3}} \right)^{-1} \times \left(\frac{L}{1000 \text{ pc}} \right) \quad (2)$$

Here, we have adopted a fiducial electron density for the ISM and assumed a path length through both the thin and thick disk. This magnetic field strength is stronger than that observed in NGC 4631 but of the same order. However, we cannot infer that such a phenomenon is present without a study similar to [Fletcher et al. \(2011\)](#) or [Mora-Partiarroyo et al. \(2019\)](#) conducted on HG 190608.

(iv) Finally, we consider that a dense and turbulent medium associated with the FRB source (i.e. a circumburst medium) gives rise to the high RM. For a region with $n_e = 5 \text{ cm}^{-3}$ and $L = 10 \text{ pc}$, we could expect the same parallel field strength as the scenario above. Though this would be an unusually powerful magnetic field, it is not unprecedented, especially in the field of FRBs.

In the case of the FRB 121102, the first FRB detected to repeat, [Michilli et al. \(2018\)](#) reported a decaying source frame rotation measure of $\text{RM}_{\text{src}} \sim 10^5 \text{ rad m}^{-2}$ and a magnetic field parallel to the line-of-sight on the order of $\sim \text{mG}$, much stronger than we have considered here for FRB 190608. [Margalit & Metzger \(2018\)](#) proposed that the progenitor of FRB 121102 could be a young magnetar embedded in a magnetized nebula. While the observables for FRB 190608 do not indicate as unique an environment, given the unknown nature of FRBs, we consider it possible that a magnetic environment related the burst or circumburst medium gives rise to the high rotation measure.

We conclude that the most likely explanation for the observed rotation measure is a combination of contributions from the host galaxy ISM and the burst/circumburst medium.

5. DISCUSSION

5.1. The Local Environment of FRB 190608

We now consider the local environment of FRB 190608 and compare its properties with the overall properties of the galaxy. First, the FRB localization is coincident with one of the two prominent spiral arms of the galaxy.

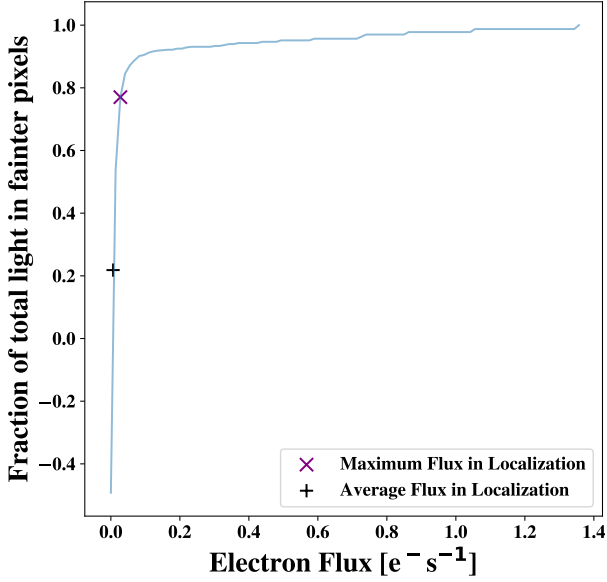


Figure 7. The figure shows the fraction of total light in pixels fainter than a given electron flux value - with fraction of light as a function of electron flux. This can be used to show relative brightness of the FRB localization. We find that the maximum brightness in the area of localization is one of the more UV bright pixels in the image but not the brightest. Here we show the fraction of light in pixels fainter than the maximum flux is approximately 0.78 - i.e., $\approx 78\%$ of the light in the image is in pixels fainter than the localization maximum, indicated by the blue cross. The burst may have occurred in a relatively bright star-forming region but not the most luminous as found with GRB local environments.

Defining these arms by the luminous UV emission (i.e. the contours in Figure 1), we estimate a chance coincidence of 20% for an event occurring within 3 effective radii of the galaxy center. Therefore, a chance association is unlikely.

While an association of FRB 190608 to a star-forming region within a spiral arm of HG 190608 is probable, we emphasize that the event did not occur in the most active star-forming region. On the other hand, Figure 7 shows a histogram of the cumulative pixel fluxes from the *HST/UVIS* image. Using a method similar to that used for GRB analysis (Fruchter et al. 2006) to compare GRB environments to supernovae environments, we calculated the fraction of total light in pixels fainter than the average and maximum pixel brightness at the FRB localization.

These fractions are calculated using

$$f = \frac{\Sigma(F_i < \text{limit})}{\Sigma F_i} \quad (3)$$

where F_i is a pixel flux, and the limit is some number between 0 and the maximum flux in the entire image. This can sometimes result in a negative fraction as seen in 7 because of negative flux values dominating the sum in the numerator. We plotted markers at specific limits associated with the FRB localization.

We estimate that, for the average flux of $0.00638 \text{ e}^- \text{ s}^{-1}$ in an elliptical aperture with axes equal to σ_{RA} and σ_{Dec} , the fraction of light in pixels fainter than this is 0.22. For the maximum flux in the localization ellipse ($0.0276 \text{ e}^- \text{ s}^{-1}$), the fraction of light in pixels fainter than this value is 0.780. (Figure 7).

Thus, the event did not occur in the brightest star-forming region of the galaxy. This contrasts with long-duration GRBs whose progenitors track the most luminous UV emission of their host galaxies (e.g. Fruchter et al. 2006; Lyman et al. 2017).

We can estimate the star-formation rate (SFR) surface density (Σ_{SFR}) at the FRB position from $\mu_{\text{H}\alpha}^{\text{corr}}$. Using the canonical $L_{\text{H}\alpha}$ -SFR relationship from Kennicutt (1998), from Section 3.2, we estimate $\Sigma_{\text{SFR,FRB}} = 1.2 \times 10^{-2} \text{ M}_{\odot} \text{ yr}^{-1} \text{ kpc}^{-2}$. This value is similar to the average SFR estimated from the $3''$ SDSS fiber covering the inner regions of the galaxy. Similar to the UV flux analysis in Figure 7, we infer no enhanced star-formation at the FRB location relative to other areas in the inner few kpc. However, we note that there is no favored environment for a progenitor when compared with overall galaxy properties (Bhandari et al. 2020).

We have searched the data for signatures of disturbance or anomalous emission in the environment of FRB 190608. We derive a modest Σ_{SFR} consistent with the emission along the spiral arms of the galaxy. Similarly, we derive an $\text{H}\beta/[\text{O III}]$ ratio at the FRB which is comparable to the remainder of the galaxy (excluding the AGN-dominated nucleus). Finally, the gas kinematics closely track the overall rotation of the galactic disk, and there is no excess velocity dispersion.

5.2. Comparison to the host of FRB 180916.J0158+65

The detection of HG 190608 offers the opportunity to compare galaxy properties with the spiral host galaxy of FRB 180916.J0158+65, a repeating fast radio burst whose localization was reported in Marcote et al. (2020).

FRB 180916.J0158+65 was associated with a star-forming clump in a $z=0.0337$ galaxy with the redshift identified from a Gemini-North long-slit spectrum. Emission lines from $[\text{N II}]$, $\text{H}\alpha$, and $[\text{O III}]$ available in their spectrum suggest the host is most likely a star-forming galaxy when considered on a BPT diagnostic plot (Baldwin et al. 1981). This is in contrast to

HG 190608, which Bhandari et al. (2020) identify as a LINER galaxy from the pPXF-processed SDSS spectrum.

The V-shaped star-forming clump associated with FRB 180916.J0158+65 suggests a perturbed environment with a projected size of about 1.5 kpc. Marcote et al. (2020) suggest that this region is likely the result of an interaction with a satellite dwarf galaxy or between multiple star-forming regions. HG 190608 has no remarkable features at the FRB position indicative of a history of galactic interactions. Marcote et al. (2020) also estimate a star formation surface density on the order of $10^{-2} \text{ M}_{\odot} \text{ yr}^{-1} \text{ kpc}^{-2}$, similar to our estimate at the location of FRB 190608.

FRB 190608 also has a Faraday rotation measure $3\times$ higher than FRB 180916.J0158+65 ($\text{RM} = -114.6 \pm 0.6 \text{ rad m}^{-2}$, CHIME/FRB Collaboration et al. 2019). While the RM of 180916.J0158+65 is more consistent with observations of M51 (Fletcher et al. 2011), we cannot exclude the possibility that both are dominated by contributions from the host ISMs.

Despite the fact that both FRB hosts are spiral galaxies, they have distinct galactic and FRB properties. The same can be said when considering the low metallicity dwarf galaxy hosting the repeating FRB 121002 (Tendulkar et al. 2017). From these global properties, we can conclude that FRBs, whether repeating or not, can occur in very different galactic environments. This may support the burgeoning thesis that FRBs have different origins and that there are distinct populations of bursts. Our results alone, however, cannot conclusively determine to which population FRB 190608 belongs.

6. CONCLUDING REMARKS

We have presented an analysis of the spiral galaxy hosting FRB 190608 in order to study the local environment with a focus on observed propagation effects of the burst. We summarize our primary results as follows:

- While the FRB is coincident with a bright star-forming region of the galaxy identified in the UV, it is not the *brightest* region, in contrast to the majority of long-duration GRB environments.
- From the inferred $\text{H}\alpha$ flux, we estimate the host galaxy ISM dispersion measure contribution to be $\text{DM}_{\text{Host,ISM}} = 82 \pm 35 \text{ pc cm}^{-3}$. From the stellar and dynamical mass measurements, we estimate a halo contribution of $\text{DM}_{\text{Host,Halo}} = 55 \pm 25 \text{ pc cm}^{-3}$, for a total $\text{DM}_{\text{Host}} = 137 \pm 43 \text{ pc cm}^{-3}$.
- The large observed scattering timescale of the burst is most likely due to a dense, turbulent H II region within the galaxy that is intersecting our

sightline. An exceptional environment with no Milky Way analog would be necessary if the scattering occurred local or very local to the burst.

- A Faraday rotation measure of $353 \pm 2 \text{ rad m}^{-2}$ would be unusually high to attribute solely to the host ISM, but not implausible. The local environment of the FRB would need to be highly magnetized and/or dense (compared to the ISM) if it were the source of the high RM. We consider the most likely case is that both the local environment and ISM contribute to the observed RM.
- HG 190608 is similar to the host of FRB 180916.J0158+65 with comparable Σ_{SFR} and morphology. But we identify no morphological, kinematic, nor emission perturbations at the location of FRB 190608.

In the absence of optical or other higher-energy counterparts to detected FRBs, galactic host analyses remain one of the most informative paths forward to identifying progenitors. We will continue our multi-wavelength investigation of HG 190608 with *HST*/IR results in future work on behalf of the *Fast and Fortunate for FRB Follow-up* (F^4)⁵ collaboration along with similar analysis for galaxies hosting well-localized FRBs.

ACKNOWLEDGEMENTS

Based on observations collected at the European Southern Observatory under ESO programmes 0102.A-0450(A) and 0103.A-0101(B). Authors J.S.C., R.A.J., S.S., A.M., J.X.P., N.T., and K.H., as members of the Fast and Fortunate for FRB Follow-up team, acknowledge support from NSF grants AST-1911140 and AST-1910471. This work is supported by the Nantucket Maria Mitchell Association. R.A.J. and J.S.C. gratefully acknowledge the support of the Theodore Dunham, Jr. Grant of the Fund for Astrophysical Research. J.S.C. would like to thank Rainer Beck for his helpful input on the magnetic fields of spiral galaxies. K.W.B., J.P.M., and R.M.S. acknowledge Australian Research Council (ARC) grant DP180100857. A.T.D. is the recipient of an ARC Future Fellowship (FT150100415). L.M. acknowledges the receipt of an MQ-MRES scholarship from Macquarie University. R.M.S. is the recipient of an ARC Future Fellowship (FT190100155). N.T. acknowledges support by FONDECYT grant 11191217. K.E.H. acknowledges the support by a Project Grant (162948051) from The Icelandic Research Fund. The Australian Square Kilometre Array Pathfinder is part

⁵ ucolick.org/f-4

of the Australia Telescope National Facility which is managed by CSIRO. Operation of ASKAP is funded by the Australian Government with support from the National Collaborative Research Infrastructure Strategy. ASKAP uses the resources of the Pawsey Supercomputing Centre. Establishment of ASKAP, the Murchison Radio-astronomy Observatory and the Pawsey Supercomputing Centre are initiatives of the Australian Government, with support from the Government of Western Australia and the Science and Industry Endowment Fund. We acknowledge the Wajarri Yamatji as the traditional owners of the Murchison Radio-astronomy Observatory site. Spectra were obtained at the W. M. Keck Observatory, which is operated as a scientific partnership among Caltech, the University of California, and the National Aeronautics and Space Administra-

tion (NASA). The Keck Observatory was made possible by the generous financial support of the W. M. Keck Foundation. The authors recognize and acknowledge the very significant cultural role and reverence that the summit of Mauna Kea has always had within the indigenous Hawaiian community. We are most fortunate to have the opportunity to conduct observations from this mountain. The NUV data are based on observations with the NASA/ESA Hubble Space Telescope obtained [from the Data Archive] at the Space Telescope Science Institute, which is operated by the Association of Universities for Research in Astronomy, Incorporated, under NASA contract NAS5- 26555. Support for Program number 15878 was provided through a grant from the STScI under NASA contract NAS5- 26555.

REFERENCES

- Avila, R. J., Hack, W., Cara, M., et al. 2015, *Astronomical Society of the Pacific Conference Series*, Vol. 495, *DrizzlePac 2.0 - Introducing New Features*, ed. A. R. Taylor & E. Rosolowsky, 281
- Baldwin, J. A., Phillips, M. M., & Terlevich, R. 1981, *PASP*, 93, 5
- Bannister, K. W., Deller, A. T., Phillips, C., et al. 2019, *arXiv e-prints*, arXiv:1906.11476
- Beck, R. 2015, *A&A Rv*, 24, 4
- Bhandari, S., Sadler, E. M., Prochaska, J. X., et al. 2020, *ApJ*, Accepted
- Bhat, N. D. R., Cordes, J. M., Camilo, F., Nice, D. J., & Lorimer, D. R. 2004, *ApJ*, 605, 759
- Bloom, J. S., Kulkarni, S. R., Price, P. A., et al. 2002, *ApJL*, 572, L45
- Brown, J. C., & Taylor, A. R. 2001, *ApJL*, 563, L31
- Cardelli, J. A., Clayton, G. C., & Mathis, J. S. 1989, *ApJ*, 345, 245
- Chatterjee, S., Law, C. J., Wharton, R. S., et al. 2017, *Nature*, 541, 58
- CHIME/FRB Collaboration, Andersen, B. C., Bandura, K., et al. 2019, *ApJL*, 885, L24
- Colombo, D., Meidt, S. E., Schinnerer, E., et al. 2014, *ApJ*, 784, 4
- Cordes, J. M., & Chatterjee, S. 2019, *ARA&A*, 57, 417
- Cordes, J. M., & Lazio, T. J. W. 2002, *ArXiv Astrophysics e-prints* arXiv:astro-ph/0207156, astro-ph/0207156
- Cordes, J. M., Wharton, R. S., Spitler, L. G., Chatterjee, S., & Wasserman, I. 2016, *arXiv e-prints*, arXiv:1605.05890
- Day, C. K., Deller, A. T., Phillips, C., et al. 2020, *MNRAS*, In prep.
- Dexter, J., Deller, A., Bower, G. C., et al. 2017, *MNRAS*, 471, 3563
- Di Teodoro, E. M., & Fraternali, F. 2015, *MNRAS*, 451, 3021
- Dressel, L. 2019, *Wide Field Camera 3 Instrument Handbook*, Version 12.0.
<https://hst-docs.stsci.edu/display/WFC3IH>
- Eftekhari, T., & Berger, E. 2017, *ApJ*, 849, 162
- Elmegreen, B. G. 1994, *ApJL*, 425, L73
- Englmaier, P., & Shlosman, I. 2000, *ApJ*, 528, 677
- Fletcher, A., Beck, R., Shukurov, A., Berkhuijsen, E. M., & Horellou, C. 2011, *MNRAS*, 412, 2396
- Foreman-Mackey, D., Hogg, D. W., Lang, D., & Goodman, J. 2013, *PASP*, 125, 306
- Fruchter, A. S., Levan, A. J., Strolger, L., et al. 2006, *Nature*, 441, 463
- Gaia Collaboration, Brown, A. G. A., Vallenari, A., et al. 2018, *A&A*, 616, A1
- Jedrzejewski, R. I. 1987, *MNRAS*, 226, 747
- Kalberla, P. M. W., & Kerp, J. 2009, *ARA&A*, 47, 27
- Katz, J. I. 2017, *MNRAS*, 471, L92
- Kennicutt, Robert C., J. 1998, *ApJ*, 498, 541
- Krishnakumar, M. A., Mitra, D., Naidu, A., Joshi, B. C., & Manoharan, P. K. 2015, *ApJ*, 804, 23
- Leroy, A. K., Schinnerer, E., Hughes, A., et al. 2017, *ApJ*, 846, 71
- Lyman, J. D., Levan, A. J., Tanvir, N. R., et al. 2017, *MNRAS*, 467, 1795
- Macquart, J.-P., Prochaska, J. X., McQuinn, M., et al. 2020, *Nature*, Accepted
- Marcote, B., Nimmo, K., Hessels, J. W. T., et al. 2020, *Nature*, 577, 190

- Margalit, B., & Metzger, B. D. 2018, *ApJL*, 868, L4
- Marnoch, L., & Ryder, S. D. 2020, *Astronomy & Astrophysics*, Submitted
- McKee, J. W., Lyne, A. G., Stappers, B. W., Bassa, C. G., & Jordan, C. A. 2018, *MNRAS*, 479, 4216
- Michilli, D., Seymour, A., Hessels, J. W. T., et al. 2018, *Nature*, 553, 182
- Mo, H. J., Mao, S., & White, S. D. M. 1998, *MNRAS*, 295, 319
- Mora-Partiarroyo, S. C., Krause, M., Basu, A., et al. 2019, *A&A*, 632, A11
- Morrissey, P., Matuszewski, M., Martin, D. C., et al. 2018, *ApJ*, 864, 93
- Moster, B. P., Naab, T., & White, S. D. M. 2013, *MNRAS*, 428, 3121
- Neeleman, M., Bañados, E., Walter, F., et al. 2019, *ApJ*, 882, 10
- Oppermann, N., Junklewitz, H., Robbers, G., et al. 2012, *A&A*, 542, A93
- Osterbrock, D. E., & Ferland, G. J. 2006, *Astrophysics of gaseous nebulae and active galactic nuclei*
- O’Sullivan, D., Martin, C., Matuszewski, M., et al. 2019, *arXiv e-prints*, arXiv:1911.10740
- Petroff, E., Hessels, J. W. T., & Lorimer, D. R. 2019, *A&A Rv*, 27, 4
- Planck Collaboration, Ade, P. A. R., Aghanim, N., et al. 2016, *A&A*, 594, A13
- Platts, E., Weltman, A., Walters, A., et al. 2019, *PhR*, 821, 1
- Prochaska, J. X., & Zheng, Y. 2019, *MNRAS*, 485, 648
- Prochaska, J. X., Bloom, J. S., Chen, H. W., et al. 2006, *ApJ*, 642, 989
- Rafelski, M., Teplitz, H. I., Gardner, J. P., et al. 2015, *AJ*, 150, 31
- Ravi, V., Catha, M., D’Addario, L., et al. 2019, *Nature*, 572, 352
- Reynolds, R. J. 1977, *ApJ*, 216, 433
- Schommer, R. A., & Sullivan, W. T., I. 1976, *Astrophys. Lett.*, 17, 191
- Simha, S., Burchett, J., Chittidi, J., et al. 2020, *ApJ*, Submitted
- Stern, J., & Laor, A. 2012, *MNRAS*, 423, 600
- Tendulkar, S. P., Bassa, C. G., Cordes, J. M., et al. 2017, *ApJL*, 834, L7
- Vieyro, F. L., Romero, G. E., Bosch-Ramon, V., Marcote, B., & del Valle, M. V. 2017, *A&A*, 602, A64
- Xu, J., & Han, J. L. 2015, *Research in Astronomy and Astrophysics*, 15, 1629
- Zhang, G. Q., & Wang, F. Y. 2019, *MNRAS*, 487, 3672